FULL PAPER

Soft Robotic Concepts in Catheter Design: an On-Demand Fouling-Release Urinary Catheter

Vrad Levering, Qiming Wang, Phanindhar Shivapooja, Xuanhe Zhao, and Gabriel P. López**

Infectious biofilms are problematic in many healthcare-related devices and are especially challenging and ubiquitous in urinary catheters. This report presents an on-demand fouling-release methodology to mechanically disrupt and remove biofilms, and proposes this method for the active removal of infectious biofilms from the previously inaccessible main drainage lumen of urinary catheters. Mature *Proteus mirabilis* crystalline biofilms detach from silicone elastomer substrates upon application of strain to the substrate, and increasing the strain rate increases biofilm detachment. The study presents a quantitative relationship between applied strain rate and biofilm debonding through an analysis of biofilm segment length and the driving force for debonding. Based on this mechanism, hydraulic and pneumatic elastomer actuation is used to achieve surface strain selectively within the lumen of prototypes of sections of a fouling-release urinary catheter. Proof-of-concept prototypes of sections of active, fouling-release catheters are constructed using techniques typical to soft robotics including 3D printing and replica molding, and those prototypes demonstrate release of mature *P. mirabilis* crystalline biofilms (e.g., ≈90%) from strained surfaces. These results provide a basis for the development of a new urinary catheter technology in which infectious biofilms are effectively managed through new methods that are entirely complementary to existing approaches.

1. Introduction

Infection of urinary catheters with bacterial biofilms is a pervasive and challenging issue in healthcare. In the USA alone, over 30 million Foley urinary catheters are used annually to treat urine retention during short-term surgical procedures as well as longer-term conditions requiring kidney dialysis, time in intensive care, or time in assisted-living facilities.[1] Catheter-associated urinary tract infections (CAUTIs) are the most common type of nosocomial infections and account for 30–40% of all hospital infections.[2] The unavoidable formation of asymptomatic biofilms in urinary catheters promotes development of symptomatic CAUTIs, and nearly 100% of patients that undergo catheterization for longer than 28 d will suffer some form of infection.[3] A biofilm can harbor bacteria for persistent infections and can also grow in thickness sufficiently to block urine flow causing trauma, leakage, polynephritis, septicemia, and shock, which lead to dangerous and expensive emergency treatments.[4] These infections are a concern for individual patients and for the public due to the implications of antibiotic resistance, and CAUTIs can represent a significant financial burden to hospitals.[5]

Biofilm formation begins with an initial layer of proteins attaching, which then facilitate the attachment of aquatic (planktonic) bacterial cells to the catheter surface.[6] Pilli often help stabilize attachment, a thin basal layer forms, and the bacteria multiply.[6] Bacterial attachment activates genes for synthesis of exopolysaccharide matrix, which has a protective effect for the bacteria, often requiring over 100 times the concentration of antibiotic to kill the bacteria compared to the liquid-borne phenotype.[6] In the case of *Proteus mirabilis*, a particularly problematic bacteria found in approximately 20% of single biofilm, and more than 30% of mixed biofilm, CAUTIs,[7] attachment also results in the production of urease, which causes crystalline biofilm encrustation akin to that of better-known kidney stones.[4,8] The urease that *P. mirabilis* generates leads to an alkaline environment, and the biofilm then incorporates calcium and magnesium phosphate crystals precipitated from the urine.[9]

Current commercially available catheters attempt to either kill or prevent adhesion of bacteria through elution of antibiotics or through incorporation of non-fouling surface treatments, but at best these measures simply delay bacterial adherence for several days. Examples of extant commercial approaches include hydrogel coatings—which still suffer from attachment and biofilm formation in less than 7 d;[3,4,10] and antibiotic-releasing or silver-ion-releasing luminal materials—which prevent biofilm formation for, at most, 7 d.[3,4,10a,c,11] Indeed, Pickard's recent

V. Levering, Q. Wang, Prof. X. Zhao, Prof. G. P. López
Research Triangle MRSEC
Duke University
Durham, NC 27708, USA
E-mail: xuanhe.zhao@duke.edu
V. Levering, P. Shivapooja, Prof. G. P. López
Department of Biomedical Engineering
Duke University
Durham, NC 27708, USA
E-mail: gabriel.lopez@duke.edu
Q. Wang, Prof. X. Zhao, Prof. G. P. López
Department of Mechanical Engineering and Materials Science
Duke University
Durham, NC 27708, USA

DOI: 10.1002/adhm.201400035

and thorough multi-center randomized trial conclusively determined that silver alloy-catheters did not effectively reduce the incidence of symptomatic CAUTIs.[12] No effective method exists on the current market to stop crystalline biofilm encrustations, and commercially available methods meant to slow biofilm formation show only limited efficacy.[3,6,10a,b,11b,13]

Here, we present a new concept for a urinary catheter capable of on-demand fouling-release, a new approach that is different from all antifouling methods used in current catheters. The new design is based on active deformation of the inner surfaces of elastomeric catheters in response to external stimuli. The mechanism employed to achieve active surface deformation is similar to that reported by Whitesides and coworkers who actuated the appendages of soft robots pneumatically.[14] In our work, we hypothesized that active surface deformation of elastomers[15] can significantly facilitate the release of encrustation by crystalline urinary biofilms. To test the hypothesis, we first developed a method to grow mature crystalline biofilms in vitro, on flat silicone substrates. We applied strains on the silicone substrates at various strain rates, and then examined the detachment of biofilms. We found that the applied strain and strain rate both have significant effects on biofilm detachment: when the applied strain rate is relatively low, biofilms will not debond from the substrates even under very high strains; instead, the biofilms are fractured into small segments that remain attached to the substrates. On the other hand, when the applied strain rate is relatively high, biofilms can be readily detached as large pieces, once the applied strain reaches a critical value. We quantified the mechanical properties of biofilms formed by *P. mirabilis* and developed a theoretical model to account for the effects of applied strain and strain rate on biofilm detachment. The model can be used to interpret the experimental phenomena, offering a potential design tool in future design of active surfaces for antifouling applications. We then used prototype fabrication techniques established for soft robotics[14a,16] to develop models of segments of urinary catheters that utilized substrate deformation by hydraulic actuation to debond *P. mirabilis* biofilms in vitro. Crystalline biofilms were effectively debonded from these prototypes, suggesting a promising option for development of a new approach to control of catheter-associated biofilms and UTIs that can augment, as well as circumvent the limitations of, current antifouling approaches used in catheter technology.

2. Results and Discussion

2.1. Concept for Urinary Catheter with Active Fouling-Release

As shown in **Figure 1**, we conceived a urinary catheter that uses regioselective actuation of soft elastomers to actively debond biofilms from its inner surfaces (Figure 1a–c). The debonded biofilm can then be removed by a minimal flow (e.g., of urine, Figure 1d), thereby removing any biofilm obstructions and clearing the urine drainage lumen. We grew crystalline biofilms on proof-of-concept prototypes and actuated the prototypes to debond and remove the biofilm (Figure 1f,g). While multiple inflation lumens are feasible for urinary catheter manufacturing (Figure 1a–d), we used a single intrawall lumen to demonstrate the concept (Figure 1e–g). The actuation was achieved on the luminal surface through inflation of an intrawall lumen that is separated from the main drainage lumen by a thin wall.

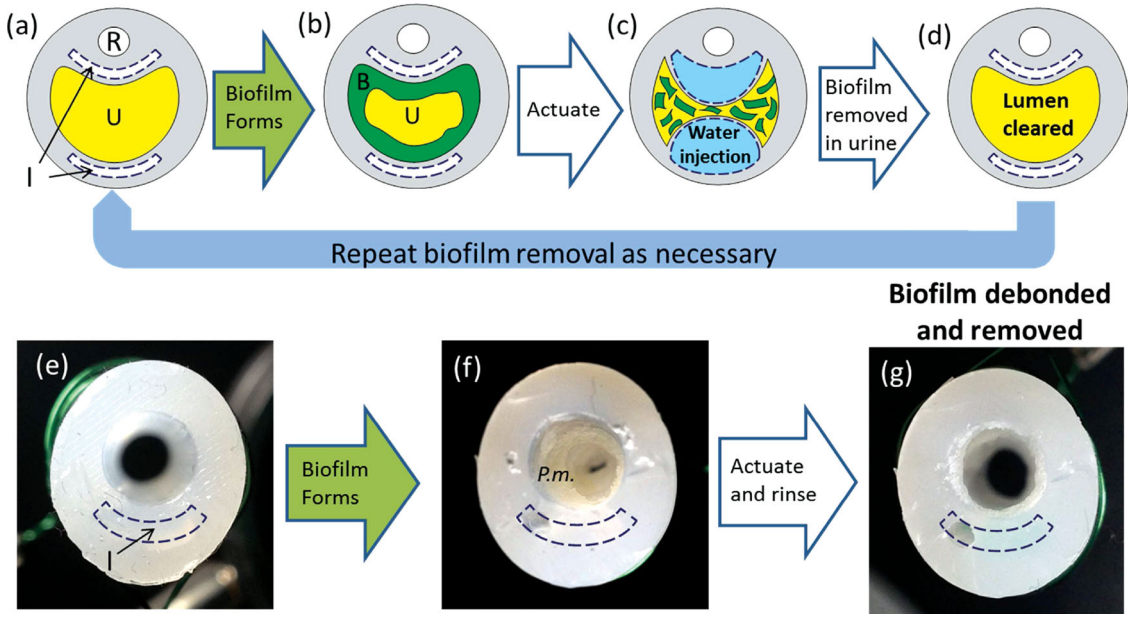

Figure 1. A conceptual schematic of the active fouling release urinary catheter and demonstration of proof-of-concept prototypes. a) Cross-section of urinary catheter before biofilm formation where R, U, and I represent the restraint balloon lumen, main urine drainage lumen and inflation lumens. b) Biofilm, denoted as B, forms on the drainage lumen. c) Reversible actuation of the lumen via water inflation debonds the biofilm formed in the urine drainage lumen. d) Debonded biofilm is carried away in the urine resulting in a cleared lumen thereby reducing risk of symptomatic infections. Optical images of proof-of-concept prototype cross-sections e) before biofilm growth, f) after growth of a mature *P. mirabilis* crystalline biofilm (*P.m.*) in the drainage lumen, and g) after actuation and a gentle rinse debonded and removed the biofilm.

When sufficient pressure is applied to the intrawall lumen(s), the thin wall stretches and generates strain on the luminal surface (Figure 1c; see also additional actuation description in Section 2.4). We first experimentally and theoretically explored the substrate-strain-induced debonding of an infectious crystalline biofilm, and then used that understanding to develop a proof-of-concept prototype of a section of an active, fouling-releasing catheter.

2.2. Uniaxial Strain Debonds Mature *P. Mirabilis* crystalline Biofilms

Before the implementation of the design in a model of a catheter, we first tested the hypothesis that active surface deformation can effectively detach crystalline urinary biofilms using flat elastomer coupons. We developed an in vitro, flat, biofilm-growth configuration to facilitate quantitative measurement of the biofilm area coverage and mechanical properties. *Proteus mirabilis* was grown on silicone substrates in a modified drip flow reactor[17] where the silicone substrate was submerged to simulate physiological conditions in a conventional silicone urinary catheter (Figure S1a, S1b, Supporting Information). We chose DragonSkin20 silicone (Smooth on, USA) to fabricate the flat silicone substrate coupons due to the similarity in mechanical properties (tensile modulus approximate 0.2 MPa) to those in commercial all-silicone catheters.[18] Artificial urine supplemented with 1% tryptic soy broth was peristaltically pumped through the reactor at 0.5 mL min^{-1} for 48 h, or until the drainage tubing occluded (average time: 42 h). The resultant biofilm included crystal deposition typical of the mature crystalline biofilms observed in occluded catheters removed from patients (**Figure 2**a, S1c, Supporting Information). Scanning electron microscope (SEM) analysis revealed the large crystals and microcrystalline aggregates that are similar to struvite and apatite crystals typically seen on SEM images of cross-sections of occluded catheters (Figure S1c, Supporting Information).[13b] The biofilm thickness (0.57 ± 0.07 mm) was measured by quantifying microscope height adjustment as the focus was adjusted from the substrate to the top of the biofilm. It was comparable to the thickness required to block catheters in previous in vitro studies.[19] System sterility was confirmed by control runs without bacterial inoculation; only minor amounts of non-adherent debris were observed and no biofilm was formed. To our knowledge, this study presents the first growth model for a mature crystalline biofilm in a flat configuration, which was then used to study biofilm debonding and biofilm mechanical properties.

We carefully removed the flat silicone samples from the reactor to avoid disturbing the integrity of the crystalline biofilm. Uniaxial strain was applied to the silicone substrates using methods similar to those established in our previous study.[15] We clamped the silicone at both longitudinal ends on a horizontal mechanical stretcher (Figure 2b), and applied strain, ε, to the silicone substrate at a rate of 0.2 s^{-1}. The samples were stretched to 35% strain 10 times, unclamped, submerged in DI water, and rinsed at 4 mL min^{-1} for 1 min. We removed the samples from the DI water and then crystal violet stained (0.1%) the biofilm for 10–15 min before two additional

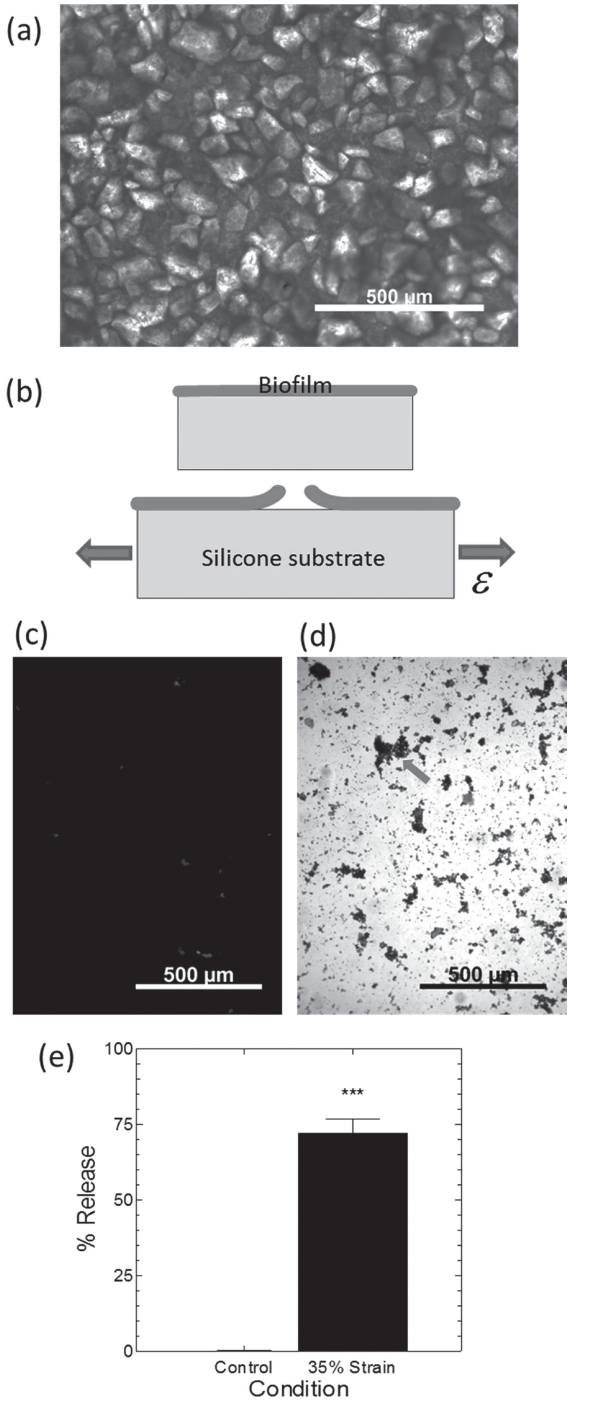

Figure 2. Debonding of mature *P. mirabilis* crystalline biofilms due to strain applied to flat silicone substrates. a) Optical microscopy image of a crystalline biofilm on a flat silicone substrate. b) Diagram (side view) illustrates tensile strain, ε, applied to the substrate causing biofilm debonding. Optical microscopy images of biofilm-covered silicone substrates c) after rinsing and staining with crystal violet, or d) after actuation to 35% strain 10 times (at 0.2 s^{-1}) before rinsing and staining. The arrow indicates an example residual island of stained biofilm that remained on the silicone substrate. e) Image analysis of biofilm area coverage confirmed that 10 cycles of 35% substrate strain caused detachment of *P. mirabilis* biofilm. Data represent mean ± standard error of the mean, $N = 3–4$. "***" denotes $P < 0.001$.

water rinses.[20] Crystal violet effectively stained and allowed quantitative assessment of the area coverage of the biofilms (Figure 2c,d).[21] The samples were imaged along the longitudinal midline, and the images were characterized for biofilm area coverage by use of image analysis to estimate the fraction of pixels in the image corresponding to crystal violet stained biofilm. We note that in the discussion here and below, the term "biofilm area coverage" is a conservative indicator of the actual amount of biofilm debonded from the sample surface because local cohesive failure of the biofilm can result in the bulk of the material being shed from the surface while small amounts of stainable biofilm are retained at the substrate surface. The 35% straining regimen applied to the substrate resulted in a reduction in the biofilm area coverage of the silicone surface of 72% (Figure 2c,d,e). These data suggest that at least 72% of the crystalline biofilm detached from the samples, and we emphasize again here that this number is a conservative indication of the amount of biofilm removed (especially when considering the >0.5 mm thickness of the initial biofilm). These results are consistent with our previous studies, which showed that straining of an elastomer can result in detachment of mucoid biofilms formed by *Escherichia coli* and *Cobetia marina*, a marine bacterium.[15] Interestingly, Limbert et al. recently conducted finite element analysis predicting biofilm debonding due to substrate micromotion caused by tension, torsion, or bending but did not provide experimental results to confirm their predictions.[22] The current work represents the first experimental observation of active debonding of a mature, crystalline biofilm (>24 h old) by strain applied to an elastomeric substrate.

2.3. High Strain and Strain Rate Result in Debonding of Mature *P. Mirabilis* Crystalline Biofilms

We next studied the effects of applied strain and strain rate on the debonding of *P. mirabilis* crystalline biofilms from flat silicone substrates. For strains ranging from 0% to 100%, the strain rate was varied across a wide range, from 0.01 to 0.4 s^{-1}; each sample was strained 10 times at its designated strain rate. As shown in **Figure 3**a, both the applied strain and the strain rate are important in eliciting the debonding of crystalline biofilms. At relatively high strain rates (i.e., 0.2 and 0.4 s^{-1}), significant amounts of biofilm are debonded (i.e., over 70%, measured using crystal violet staining as described above) as the applied strain reaches critical values (e.g., 20%–30%). However, at relatively low strain rates (i.e., 0.01 and 0.04 s^{-1}), the debonded biofilm area is insignificant (i.e., less than 10%), even when the substrate is under strains up to 100%.

We measured the storage and loss moduli of the crystalline biofilms with a frequency sweep rheometer. Although biofilms are typically viscoelastic,[23] we found that the mature crystalline biofilms generated by *P. mirabilis* in vitro appeared to be predominantly elastic (Figure S2a, Supporting Information), with a constant storage modulus G' of approximately 1.5×10^4 Pa

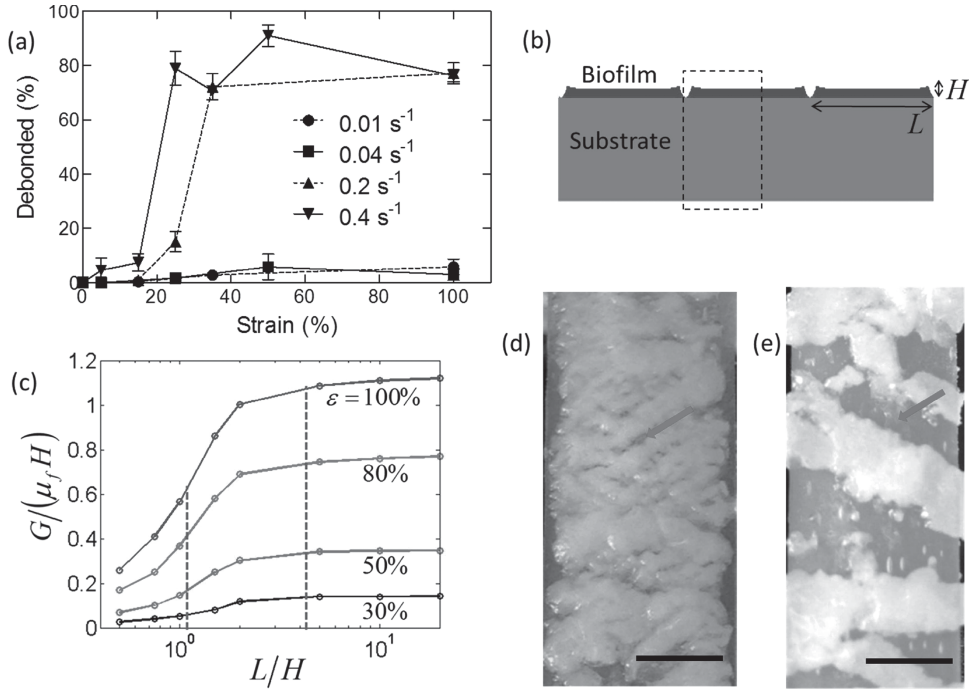

Figure 3. Increased debonding of mature *P. mirabilis* crystalline biofilms due to increased strain rate. a) The percentage of biofilm area covering the substrate (see text for details) after straining (10 times) at various strain rates. Experiments were conducted for 2–4 replicates per condition. Dashed lines indicate strain testing using LRX tensile tester and solid lines indicate strain testing using modified syringe pump. Data represents mean ± standard error of the mean. b) Diagram of biofilm height, H, and segment length, L, used for c) modeling the driving force for biofilm debonding as a function of L/H. Dashed vertical lines indicate normalized segment length for 0.01 and 0.4 s^{-1} strain rates that were measured from optical images during 100% strain at d) 0.01 s^{-1} and e) 0.4 s^{-1}. Arrows indicates examples of cracked biofilm or areas of silicone substrate exposed by debonded biofilm. Scale bars indicate 5 mm.

for low sweep frequencies (0.1–6 Hz) that was also higher than the loss modulus (approximately 4.5×10^3 Pa).[24] *Pseudomonas aureginosa* biofilms have demonstrated similar predominantly elastic properties within the same frequency range,[24,25] but the storage modulus of mature *P. mirabilis* crystalline biofilms ($\approx 1.5 \times 10^4$ Pa) was higher than that measured by Lahaye et al. for *P. mirabilis* biofilms (G' of 0.9–1.0×10^3 Pa).[26] The higher storage modulus is likely due to the integration of rigid crystals in the biofilms; similar phenomena of modulus enhancement have been observed in rigid particle filled polymers.[27] Lahaye and co-workers only tested the proteinaceous component of *P. mirabilis* biofilms and did not use growth media that would support crystal generation.[26] While a wide range of viscoelastic properties for biofilms have been reported, overall the storage modulus of mature crystalline *P. mirabilis* biofilms is 1–3 orders of magnitude greater than other clinically relevant biofilms.[28]

To better understand the effects of applied strain rates on the debonding of biofilms, we then developed a theoretical model that relates the fracture of biofilms into segments to the segments' subsequent debonding from the substrate. With a mature biofilm attached on the substrate, we stretched the substrate at a specified rate. Upon stretching, the biofilm first formed channel-like cracks, which then branched to form fragmented segments of biofilm with an average length, L.[29] Upon deformation of the substrate, cracks nucleated at the bottom of each segment, propagated through the interface between the biofilm and the substrate, and eventually debonded the biofilm from the substrate. We constructed a simplified, 2D, plane-strain model of the system of biofilm segments on the elastomer substrate as illustrated in Figure 3b. The biofilm and substrate were modeled as Neo-Hookean materials; the shear moduli (μ_f for the biofilm and μ_s for the substrate) were extracted from the measured storage moduli at near-zero frequency (Figure S2, Supporting Information).[30] The thickness of the substrate was taken to be much larger (>20 times) than that of the biofilms, H. Considering the periodicity and symmetry of the model, only half of one biofilm segment was analyzed, as indicated in the dashed box in Figure 3b. The energy release rate G (not to be confused with G' and G'' storage and loss moduli) was computed by a commercial finite element package Abaqus 6.10.1 (SIMULIA, USA). The modeling results suggest that the average segment length L plays a critical role in the biofilm debonding process.

We believe our method will be effective regardless of the crystalline content of the biofilm. The energy release rate scales as: $G \propto \mu_f \varepsilon^2 H$. A higher percentage crystallinity of the biofilm will lead to a higher shear modulus,[27] which will increase the energy release rate under the same applied strain, and thereby increase the driving force for debonding the biofilm.[31] Conversely, as the percentage of crystals in the biofilm decreases, the biofilm becomes more like mucoid biofilms such as those formed by *C. marina* and *E. coli*, which we have previously studied and have demonstrated can also be debonded by application of strain to elastomeric substrates.[15]

As shown in Figure 3c, the normalized energy release rate, $G/(\mu_f H)$, which is the driving force for biofilm debonding,[31] increases with the normalized segment length, L/H, for various applied strains in the substrate. These curves can be qualitatively understood as follows: if the biofilm segment length is very small, the segments can be regarded as tall plates vertically attached on the substrate, which result in a relatively low energy release rate.[32] When $L/H \to 0$, the driving force for biofilm debonding $G/(\mu_f H) \to 0$. On the other hand, if the biofilm segment is infinitely long, it can be regarded as a film attached on the substrate. Therefore, when $L/H \gg 1$, the driving force for biofilm debonding approaches its maximum, that is, $G/(\mu_f H) = [(1+\varepsilon)^2 + (1+\varepsilon)^{-2} - 2]/2$.[15,33] Therefore, the driving force for biofilm debonding increases with biofilm segment length, from 0 for very narrow segments to a plateau of $[(1+\varepsilon)^2 + (1+\varepsilon)^{-2} - 2]/2$ for very wide segments.

We noted that images gathered during strain testing revealed differences in typical segment length (Figure 3d,e) that correlated to strain rate. Actuation with low strain rates (i.e., 0.01 and 0.04 s^{-1}) tended to fracture the biofilm into small segments that maintained attachment on substrates (Figure 3e), while high strain rates (i.e., 0.2 and 0.4 s^{-1}) resulted in relatively large pieces of biofilms that were easily detached (Figure 3d,e; both samples at 100% strain). We quantified the segment length at 100% strain for different loading rates from representative images (Figure S4, Supporting Information), which confirmed that segment length increased monotonically as strain rate increased over the conditions studied. In Figure 3c, the dashed lines are the measured segment lengths for highest and lowest strain rates at 100% strain. The larger segment length ($L/H \approx 4.2$), given by the highest strain rate, correlates to a sufficiently high driving force to debond most of the biofilm from the substrate. Conversely, the smaller segment width ($L/H \approx 1$) for the lowest strain rate correlates to a low driving force for debonding that is not large enough to detach the biofilms from the substrate. As a result, the high strain rates lead to a higher percentage of debonded biofilm, while low strain rates debond low percentages of biofilm. The current study gives the first demonstration that the rate of the strain applied to the substrate significantly influences biofilm debonding, and the calculated relationship of segment length to debonding driving force represents a macroscale interpretation of the effect of strain rate.

2.4. Development of a Proof-of-Concept Prototype Urinary Catheter Incorporating Substrate Deformation via Intrawall Inflation

Our interest in debonding crystalline biofilms was motivated by the desire to translate the active biofouling management method[15] into tubular devices such as urinary catheters. We first applied strain axially to tubular silicone substrates to debond crystalline biofilms that were grown within their lumens (Figure S5, Supporting Information). Application of an axial strain (50% strain at a rate of 1.7 cm s^{-1}) effectively debonded the intraluminal crystalline biofilms (Figure S5c, Supporting Information). While this result demonstrates effective biofilm debonding, applying strain axially by extending the length of a catheter might not be practical in a point-of-care setting.

In order to incorporate our methods for biofilm release into technologies suitable for implementation in healthcare settings, we suggest another catheter design capable of actively

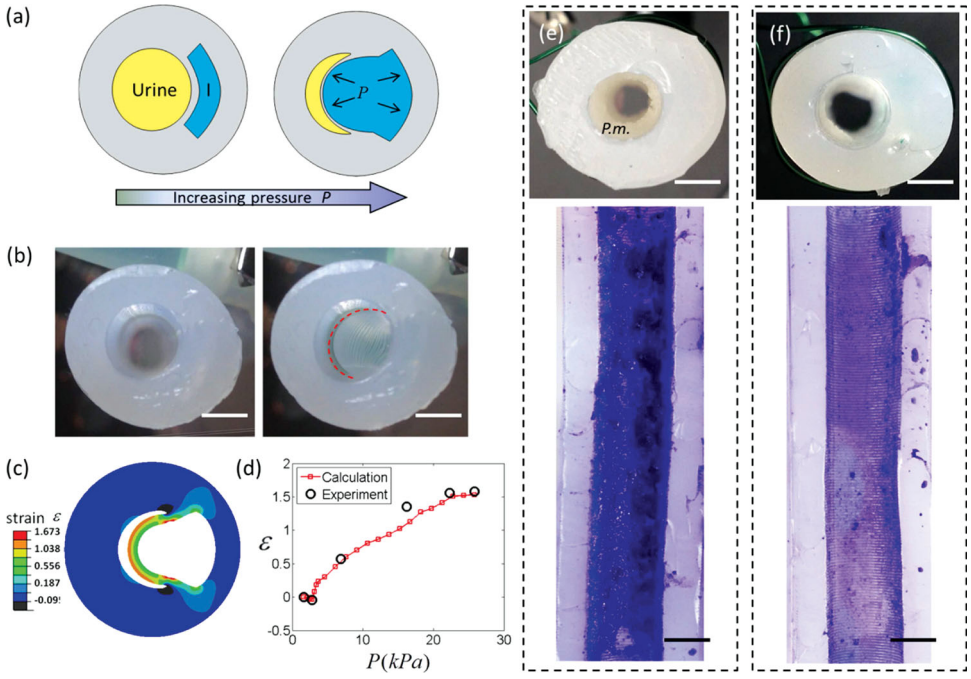

Figure 4. Proof-of-concept prototype urinary catheters debonding mature *P. mirabilis* crystalline biofilms using inflation-generated strain at urinary lumen surface. a) Schematic diagram of the prototype catheter (cross-section). Increased pressure in intrawall, inflation lumen, I, causes wall to stretch into the urine drainage lumen. b) Cross-sectional views of prototypes before and after inflation. Dashed red line outlines the inflated luminal surface. c) Maximum principal strain at the luminal surface was calculated using finite element modeling. d) Experimental and calculated luminal surface strain as a function of inflation pressure for Dragon Skin 0020 prototypes. Representative optical images from 3 to 4 replicates of e) uninflated control prototypes rinsed at 4 mL min^{-1} for 1 min, and f) prototypes inflated 10 times at 0.1 s^{-1} during rinsing demonstrate biofilm removal from actuated prototypes. Cross section of control e) shows substantial biofilm coverage (*P.m.*) after rinsing. Prototypes were stained with crystal violet and sliced open, and biofilm was removed along the length of the inflated area of the luminal surface of actuated prototypes. Scale bar indicates 2.5 mm.

debonding urinary biofilms by applying hydraulic actuation within a catheter. We conceptualized a method, similar to those used in the implementation of pneumatic networks for soft robotics,[14a] to apply strain to the catheter solely along its luminal walls, where the strain would debond urinary biofilms on the luminal surfaces without affecting the external dimensions of the catheter. **Figure 4**a shows a schematic of a proof-of-concept prototype catheter cross section with an intrawall lumen separated by a thin wall from the main, urine drainage lumen. As pressure is increased in the intrawall lumen, it inflates and the thin wall deforms and the main luminal surface strains, until it impinges on the opposite wall of main lumen (Figure 4b). To make physical, proof-of-concept models (herein referred to as prototypes) of sections of such a urinary catheter, we constructed molds for pourable silicone using 3D printing (Figure S6, Supporting Information), which allowed rapid, iterative prototype development. Our early proof-of-concept prototyping efforts varied intrawall luminal shape and position, and confirmed that using circular intrawall lumens or crescent intrawall lumens positioned too far from the main lumen resulted in non-specific wall deformation. We achieved preferential deformation of the wall between the inflation and main lumen into the main lumen by constructing thicker external walls. Figure 4b shows uninflated and pneumatically inflated prototypes. We then numerically calculated the strain within the cross-section of the prototypes using the finite element package Abaqus, while assuming the silicone was an Arrude–Boyce material[34] with a shear modulus μ_s of 221 kPa (Figure S7, Supporting Information). Model results confirmed that the inflated wall can easily achieve substrate strains sufficient to debond crystalline biofilms (e.g., greater than 30% strain, Figure 3a) over an area corresponding to approximately 40% of the perimeter of the main lumen of the prototype (Figure 4c). We again used Abaqus to calculate the inflation pressures necessary to achieve given amounts of wall strain, and the model matched well with experimental data (Figure 4d). Inflation occurred along approximately 70% of the length of the prototype catheter sections, and was limited by our methods for sealing the inflation lumen of the prototypes. No prototypes experienced failure due to wall tears and no hysteresis was observed (Figure S7, Supporting Information). We were able to attain complete inflation and deflation within 1 s. Prototypes were easily inflated pneumatically or hydraulically, and strain was controllable through pressure or volume control (Figure 4d and Table S1, Supporting Information).

2.5. Proof-of-Concept Prototypes Utilizing Intrawall Inflation Debond Mature *P. Mirabilis* Biofilm

We modified the artificial bladder biofilm growth model pioneered by Stickler and co-workers[35] to feed infected artificial urine downward through prototypes (Figure S9, Supporting Information, for flow schematic) at a rate of 0.5 mL min^{-1}, and

after approximately 42 h achieved uniform biofilm distribution around the perimeter and down the length of the main lumen (see Figure 4e for control sample). We switched to the artificial bladder growth system from the drip flow reactor system because the drip flow reactor mounting fixtures caused bubble formation and subsequent non-uniform biofilm growth in the prototypes. All biofilm growth was conducted in a sterile biosafety cabinet and the artificial bladder growth system sterility was confirmed by control runs without bacterial inoculation; no deposition was observed and no biofilm was formed on control samples. Once a mature biofilm formed on the prototypes, we carefully removed the prototypes from the growth model before rinsing them at 4 mL min^{-1} for 1 min (Figure S9b, Supporting Information). We note that, although urine voiding reaches quite high flow rates, catheters are always "open," and therefore flow rates are dominated by urine production rates. Normal urine production rates vary from 0.5 to 1.7 mL min^{-1}, but oral water loads of 8–12 mL kg^{-1} (i.e., 560–840 mL for a 70 kg individual) can cause urine production rates in excess of 10 mL min^{-1}.[36] A rinse rate of 4 mL min^{-1} is well within the urine production rates achievable through oral loading.

Thirty seconds into the rinse, prototypes designated for inflation were inflated 10 times to 35% strain at approximately 0.1 s^{-1}. The 10x inflation cycles, quite dramatically, produced visible biofilm debris in the effluent (Figure S10a and Video S1, Supporting Information) and subsequent examination of the cross-section showed that a large portion of the biofilm was removed (see Figure 4f for a representative cross-section). No "backflow" was observed (i.e., the inflation did not cause fluid to eject/flow out the top of the prototype). Biofilms in control and inflated prototypes were stained with crystal violet before the prototypes were sliced open. We confirmed that biofilm had been removed from strained areas (Figure 4f) while biofilm remained bonded to the unstrained areas. We then analyzed microscopic images of the biofilm area coverage using ImageJ and confirmed significant biofilm removal (approximately 84% of the biofilm removed from strained areas of the lumen versus 7% removed from unstrained areas; Figure S11, Supporting Information). Again, area coverage measurements appeared to understate the magnitude of biofilm removal, so the effluent collected during the rinse/inflation test was assessed for biofilm mass (Figure S10c, Supporting Information). An average of 0.29 g was removed from three inflated prototypes, which when compared to the total mass of biofilm in a control prototype (0.6 g) suggests that greater than 90% of the biofilm mass was removed from the inflated side of the sample. As illustrated in Figure 1, an additional inflation lumen would allow biofilm removal around the complete perimeter of the luminal surface and we are exploring prototypes with multiple inflation lumens for future evaluation.

3. Conclusions

We showed that surface deformation can result in debonding of crystalline biofilms and developed the first macroscale quantitative relationship between strain rate, biofilm segment length, and biofilm debonding. We then extrapolated from actuation techniques used in soft robotics to develop a method for on-demand removal of biofilms from catheters that can be applied in the previously inaccessible main lumen.[37] The mechanical biofilm-removal method circumvents the many chemical and biological issues with previous approaches to biofouling control in catheters[23b,36–38] and is complementary to bactericidal and physicochemical approaches towards biofilm-resistant surfaces.[15] This active biofouling removal method presents a promising and affordable infection control option for urinary catheters, inexpensive devices relatively unchanged for 50 years due to the complexity and expense of previous infection control efforts.[3,4] A urinary catheter with on-demand biofouling release would be valuable to the subset of patients dealing with serial, occlusive catheter blockages,[11b] but even more beneficial to society if used to proactively remove asymptomatic biofilms that lead to symptomatic CAUTIs.[3,4,13b,23b] Existing extrusion techniques are thoroughly capable of adding an intrawall inflation lumen, or even multiple inflation lumens, to catheter shafts without affecting the shafts' external dimensions. Multiple inflation lumens would allow actuation of the entire luminal surface, and inflation lumen(s) could be inflated via an additional hub port for actuation. Finally, the combination of this work with previous demonstrations of mucoid *E. coli* and *C. marina* biofilm debonding provides compelling evidence of the utility of a substrate-strain biofilm debonding method in a variety of applications.

4. Experimental Section

Bacteria Strain and Culture Media: Proteus mirabilis 2573 (ATCC 49565) was thawed from frozen stock and cultivated overnight at 37 °C on a tryptone soya broth agar slant, which was stored at 4 °C and used for up to 2 weeks. Artificial urine was prepared per the recipe originally described in Griffith and modified by Ciach and was composed of calcium chloride 0.49 g L^{-1}, magnesium chloride hexahydrate 0.65 g L^{-1}, sodium chloride 4.6 g L^{-1}, disodium sulfate 2.3 g L^{-1}, trisodium citrate dihydrate 0.65 g L^{-1}, disodium oxalate 0.02 g L^{-1}, potassium dihydrogen phosphate 2.8 g L^{-1}, potassium chloride 1.6 g L^{-1}, ammonium chloride 1.0 g L^{-1}, urea 25 g L^{-1}, and gelatin 5.0 g L^{-1} in deionized water.[19a] The medium was adjusted to a pH of 6.1 and then sterilized. Tryptone soya broth was prepared separately, sterilized, and added to the artificial urine to a final concentration of 1.0 g L^{-1}; this made the total artificial urine media (AUM). A colony of *P. mirabilis* was inoculated into 75 mL of AUM and grown for 4 h at 37 °C on a shaker at 240 rpm.

Preparation of Silicone Coupons: Flat silicone samples (Dragon Skin 0020, Smooth-On, Inc.) were manufactured by pouring 10 mL of silicone into a 90-mm diameter petri dish (VWR) generating a 1.7-mm thick silicone layer. Coupons were trimmed into 24 mm × 75 mm dimensions that would fit in a drip flow reactor (Figure S1b, Supporting Information). The coupons were removed from the petri dishes in the biosafety cabinet after rinsing with 95% ethanol and sterilized water.

Preparation of Proof-of-Concept Prototypes: Silicone prototype samples (Dragon Skin 0020 and Ecoflex 0050, Smooth-On, Inc.) were prepared by pouring approximately 10 mL of silicone into a mold prepared by a 3D printer (Dimension sst 1200es, with patterns generated using Solidworks 2011, Figure S6, Supporting Information). Silicone was degassed for 3 min prior to pour. Once cured, prototypes were removed from the molds and then the inflation lumens were sealed with additional silicone. Dragon Skin 0020 silicone prototypes were used for modeling and initial characterization including video and image analysis of inflation profiles in combination with pressure and volume measurements. Ecoflex 0050 silicone samples were also characterized, and then used for biofilm growth due to Ecoflex 0050's superior pour performance and more consistently successful molding. Before biofilm

growth, the samples were sterilized in a biosafety cabinet by rinsing with 95% ethanol and sterilized water.

Biofilm Growth: The drain of a drip flow reactor (BioSurface Technologies Corporation) was modified to keep flat silicone coupons submerged in 0.3–0.6 cm media while under flow (Figure S1, Supporting Information). The reactor and all associated supply and drain tubing were sterilized and placed in a Class II biosafety cabinet. The reactor was maintained at 37 °C by placing it in a mini-incubator. AUM was introduced using a peristaltic pump to prime the flow system. The samples in the reactor were infected with 10 mL of the 4 h *P. mirabilis* culture and the infected culture was left for 1 h to allow bacterial attachment before the media supply was resumed. The model was run continuously at a flow rate of 0.5 mL min^{-1} until the desired time point, or a system blockage occurred.

Biofilms on proof-of-concept prototypes were grown using the same flow loop and method, but the drip flow reactor was replaced with a manifold of four artificial bladders in a vertical orientation (Figure S9, Supporting Information). The bladders were maintained at 37 °C by a mini-incubator. The bladders each held a 30-mL reservoir of infected media that would overflow into glass tubing and then drip-feed through the prototypes as fresh media were added to the bladder. Again, the model was run continuously at a flow rate of 0.5 mL min^{-1} until the desired time point, or a system blockage occurred.

Strain and Inflation Testing: Biofilm-covered silicone coupons were removed from the reactor and kept covered in a hydrated state. The coupons were carefully sliced longitudinally to bisect the coupon (12 mm × 75 mm) while avoiding disturbance of the biofilm. Resultant samples were stretched to the desired strain percentage at controlled strain rates; samples were spritzed with DI water to maintain hydration during strain testing. The gauge length was 5 cm, and the sample was 1.2 cm wide. Samples were subjected to 10 strain cycles and representative videos and images were captured during testing. Two different stretchers were required to apply strains across the range of strain rates. A tensile tester with grips oriented vertically (LRX Model 400c) was used for strain rates of 0.01 and 0.2 s^{-1} (velocities of 0.2 and 1 cm s^{-1}); while a syringe pump modified with additional clamps was used for the slowest and fastest strain rates 0.04 and 0.4 s^{-1} (velocities 0.05 and 2 cm s^{-1}) due to speed limitations of the LRX tensile tester (see dashed and solid lines, respectively, in Figure 3a). Once strain tested, samples were immediately submerged in DI water and subjected to 4 mL min^{-1} flow for 1 min. Samples were then stained with 0.01% crystal violet for 10–15 min and rinsed three times with DI water. Each sample was imaged at least six times (at center of sample to eliminate edge effects), and each image was analyzed using ImageJ version 1.43u (http://rsbweb.nih.gov/ij/). ImageJ's threshold function was used to render each grayscale image into a binary image with distinct areas with and without biofilm. The threshold value supplied by imageJ was used as default (based on the IsoData algorithm), but when necessary the threshold value was manually adjusted until all visible biofilm was included within the threshold; typically, it was adjusted to account for variation in background brightness caused by partial staining of the underside/non-biofilm face of the silicone substrate. ImageJ's area measurement function was then used to quantify the area of the pixels above the threshold, and to thereby quantify the biofilm area coverage for a given image. The images' area coverage was then averaged for each sample.

Proof-of-concept prototype samples were removed from the reactor and kept covered in a hydrated state. The samples were mounted vertically, and DI water was introduced from the upper end at 4 mL min^{-1} flow for 1 min (Figure S9b, Supporting Information). Samples intended for inflation were inflated 10 times at 0.1 s^{-1} to 35% strain approximately 30 s into the 1 min rinse. Inflation was conducted hydraulically using a syringe-delivered pre-determined volume of water. Control and inflated samples were stained with crystal violet, rinsed with DI water at 4 mL min^{-1} flow for 30 s, and then filleted open for examination.

Statistical Analysis: Group means were compared by unpaired *t*-test with Welch's correction to account for potentially unequal variances. "***" denotes $P < 0.001$ where shown in figures. Data are presented as mean ± SEM (standard error of the mean) in the figures and text to account for differences in number of replicates.

Rheology Tests of Biofilms and Substrates: Circular pieces (8 mm) were punched out of biofilm-covered silicone coupons and sweep tested on a flat-plate rheometer (Rheology Advantage Instrument ARG2, USA). During the tests, the applied strain was controlled to oscillate from 0 to 0.02. Bare silicone pieces (without biofilm covering) were separately tested as controls; their storage and loss modulus values were subtracted from the biofilm-covered samples to isolate biofilm storage and loss modulus values. The modulus of biofilms and the substrates are presented in Figure S2 (Supporting Information).

Finite Element Calculations: The boundary conditions for the calculation of energy release rate in Figure 3c are illustrated in Figure S3 (Supporting Information). The thickness of the substrate, H_s, was set as 30 times the biofilm thickness, H. In Abaqus, both the biofilm and substrate were modeled as as nearly incompressible Neo-Hookean materials, and discretized as reduced integration 2D quadrilateral elements (CPE8R). The number of elements used in the model ranged from 12 000 to 40 000. The insensitivity of the model to mesh was validated by refining the mesh size of the model. The energy release rate was calculated $G = \lim_{a \to 0} \partial U / \partial a$ as, where U was the strain energy of the model, and a was the crack length as shown in Figure S3 (Supporting Information).

Figure S8 (Supporting Information) presents the model and boundary conditions for the calculation of strain at the luminal surface of the proof-of-concept prototypes in Figures 4c,d (Dragon Skin 0020 silicone). A cross-section of the prototype was modeled as an Arruda-Boyce material (parameters obtained in Figure S7, Supporting Information). The main lumen was centered for simplicity. The model was discretized as described above with 21 600 elements. The insensitivity of the model to mesh was validated by refining the mesh size of the model. The principal strain was then calculated by $\varepsilon = \exp(LE)$-1, where LE is the logrithmic strain exported from ABAQUS.

Supporting Information

Supporting Information is available from the Wiley Online Library or from the author.

Acknowledgements

V.L. and Q.W. contributed equally to this work. Funding for this work was provided by the NSF's Research Triangle Materials Research Science and Engineering Center (DMR-1121107), the Office of Naval Research (N0014-13-1-0828), and NIH Training Grant #5T32GM008555-18. The authors would like to thank Howard Levinson, M.D. for sharing his clinical perspective and Johan Adami for his assistance with 3D printing.

Received: January 15, 2014
Revised: February 24, 2014
Published online: March 25, 2014

[1] a) C. V. Gould, CDC: Guidelines for Prevention of Catheter-Associated Urinary Tract Infections 2009, http://www.cdc.gov/hicpac/pdf/CAUTI/CAUTIguideline2009final.pdf (accessed: January, **2014**) ;b) R. M. Donlan, *Clin. Infect. Dis.* **2001**, *33*, 1387; c) J. Pace, M. Rupp, R. Finch, in *Biofilms, Infection and Antimicrobial Therapy*,Taylor and Francis Group, CRC Press, London **2006**.
[2] M. T. Paradzik, B. Levojevic, A. Gabric, *Lijec. Vjesn.* **2011**, *133*, 15.
[3] D. M. Siddiq, R. O. Darouiche, *Nat. Rev. Urol.* **2012**, *9*, 305.
[4] D. J. Stickler, *Nat. Clin. Pract. Urol.* **2008**, *5*, 598.
[5] R. D. Scott, CDC: Direct Medical Costs of Healthcare Acquired Infections and Benefits of Prevention, http://www.cdc.gov/hai/pdfs/hai/scott_costpaper.pdf (accessed: January, **2014**).

[6] N. S. Morris, D. J. Stickler, R. J. McLean, *World J. Urol.* **1999**, *17*, 345.
[7] S. M. Macleod, D. J. Stickler, *J. Med. Microbiol.* **2007**, *56*, 1549.
[8] a) D. J. Stickler, J. B. King, C. Winters, S. L. Morris, *J. Infect.* **1993**, *27*, 133; b) B. D. Jones, H. L. Mobley, *J. Bacteriol.* **1989**, *171*, 6414.
[9] A. J. Cox, D. W. Hukins, *J. Urol.* **1989**, *142*, 1347.
[10] a) N. S. Morris, D. J. Stickler, C. Winters, *Br. J. Urol.* **1997**, *80*, 58; b) N. Sabbuba, G. Hughes, D. J. Stickler, *BJU Int.* **2002**, *89*, 55; c) N. S. Morris, D. J. Stickler, *J. Hosp. Infect.* **1998**, *39*, 227.
[11] a) T. M. Hooton, S. F. Bradley, D. D. Cardenas, R. Colgan, S. E. Geerlings, J. C. Rice, S. Saint, A. J. Schaeffer, P. A. Tambayh, P. Tenke, L. E. Nicolle, *Clin. Infect. Dis.* **2010**, *50*, 625; b) S. D. Morgan, D. Rigby, D. J. Stickler, *Urol. Res.* **2009**, *37*, 89.
[12] R. Pickard, T. Lam, G. MacLennan, K. Starr, M. Kilonzo, G. McPherson, K. Gillies, A. McDonald, K. Walton, B. Buckley, C. Glazener, C. Boachie, J. Burr, J. Norrie, L. Vale, A. Grant, J. N'Dow, *Lancet* **2012**, *380*, 1927.
[13] a) D. Stickler, R. Young, G. Jones, N. Sabbuba, N. Morris, *Urol. Res.* **2003**, *31*, 306; b) D. J. Stickler, S. D. Morgan, *J. Hosp. Infect.* **2008**, *69*, 350.
[14] a) F. Ilievski, A. D. Mazzeo, R. F. Shepherd, X. Chen, G. M. Whitesides, *Angew. Chem. Int. Ed.* **2011**, *50*, 1890; b) C. Majidi, *Soft Robotics* **2013**, *1*, 5.
[15] P. Shivapooja, Q. Wang, B. Orihuela, D. Rittschof, G. P. Lopez, X. Zhao, *Adv. Mater.* **2013**, *25*, 1430.
[16] R. F. Shepherd, F. Ilievski, W. Choi, S. A. Morin, A. A. Stokes, A. D. Mazzeo, X. Chen, M. Wang, G. M. Whitesides, *Proc. Natl. Acad. Sci. U.S.A.* **2011**, *108*, 20400.
[17] D. M. Goeres, L. R. Loetterle, M. A. Hamilton, R. Murga, D. W. Kirby, R. M. Donlan, *Microbiology* **2005**, *151*, 757.
[18] a) C. Villanueva, S. G. Hossain, C. A. Nelson, *J. Endourol.* **2011**, *25*, 841; b) R. Bayston, L. E. Fisher, K. Weber, *Biomaterials* **2009**, *30*, 3167.
[19] a) K. A. Kazmierska, R. Thompson, N. Morris, A. Long, T. Ciach, *Urology* **2010**, *76*, 515 e515; b) G. L. Jones, A. D. Russell, Z. Caliskan, D. J. Stickler, *Eur. Urol.* **2005**, *48*, 838; c) S. Malic, M. G. Waters, L. Basil, D. J. Stickler, D. W. Williams, *J. Biomed. Mater. Res. B Appl. Biomater.* **2012**, *100*, 133.
[20] S. Croes, R. H. Deurenberg, M. L. Boumans, P. S. Beisser, C. Neef, E. E. Stobberingh, *BMC Microbiol.* **2009**, *9*, 229.
[21] S. Favre-Bonte, T. Kohler, C. Van Delden, *J. Antimicrobiol. Chemother.* **2003**, *52*, 598.
[22] G. Limbert, R. Bryan, R. Cotton, P. Young, L. Hall-Stoodley, S. Kathju, P. Stoodley, *Acta Biomater.* **2013**, *9*, 6641.
[23] a) S. Aggarwal, R. M. Hozalski, *Langmuir* **2012**, *28*, 2812; b) L. Hall-Stoodley, J. W. Costerton, P. Stoodley, *Nat. Rev. Microbiol.* **2004**, *2*, 95.
[24] A. E. Ehret, M. Bol, *J. R. Soc. Interface* **2012**.
[25] O. Lieleg, M. Caldara, R. Baumgartel, K. Ribbeck, *Soft Matter* **2011**, *7*, 3307.
[26] E. Lahaye, T. Aubry, V. Fleury, O. Sire, *Biomacromolecules* **2007**, *8*, 1228.
[27] a) S. Stankovich, D. A. Dikin, G. H. B. Dommett, K. M. Kohlhaas, E. J. Zimney, E. A. Stach, R. D. Piner, S. T. Nguyen, R. S. Ruoff, *Nature* **2006**, *442*, 282; b) J. S. Bergstrom, M. C. Boyce, *Rubber Chem. Technol.* **1999**, *72*, 633.
[28] a) P. C. Lau, J. R. Dutcher, T. J. Beveridge, J. S. Lam, *Biophys. J.* **2009**, *96*, 2935; b) M. Bol, A. E. Ehret, A. Bolea Albero, J. Hellriegel, R. Krull, *Crit. Rev. Biotechnol.* **2013**, *33*, 145.
[29] Z. C. Xia, J. W. Hutchinson, *J. Mech. Phys. Solids* **2000**, *48*, 1107.
[30] Q. Wang, X. Zhao, *Phys. Rev. E Stat Nonlin. Soft Matter Phys.* **2013**, *88*, 042403.
[31] J. W. Hutchinson, Z. Suo, *Adv. Appl. Mech.* **1992**, *29,* 63.
[32] V. R. Thalladi, A. Schwartz, J. N. Phend, J. W. Hutchinson, G. M. Whitesides, *J. Am. Chem. Soc.* **2002**, *124*, 9912.
[33] N. S. Lu, J. I. Yoon, Z. G. Suo, *Int. J. Mater. Res.* **2007**, *98*, 717.
[34] E. M. Arruda, M. C. Boyce, *J. Mech. Phys. Solids* **1993**, *41*, 389.
[35] D. J. Stickler, N. S. Morris, C. Winters, *Methods Enzymol.* **1999**, *310*, 494.
[36] a) M. Burnier, B. Rutschmann, J. Nussberger, J. Versaggi, S. Shahinfar, B. Waeber, H. R. Brunner, *Hypertension* **1993**, *22*, 339; b) A. Zanchi, A. Chiolero, M. Maillard, J. Nussberger, H. R. Brunner, M. Burnier, *J. Clin. Endocrinol. Metab.* **2004**, *89*, 1140.
[37] C. Sousa, M. Henriques, R. Oliveira, *Biofouling* **2011**, *27*, 609.
[38] C. E. Armbruster, H. L. Mobley, *Nat. Rev. Microbiol.* **2012**, *10*, 743.

ADVANCED HEALTHCARE MATERIALS

Supporting Information

for *Adv. Healthcare Mater.*, DOI: 10.1002/adhm.201400035

Soft Robotic Concepts in Catheter Design: an On-Demand Fouling-Release Urinary Catheter

Vrad Levering, Qiming Wang, Phanindhar Shivapooja, Xuanhe Zhao, and Gabriel P. López**

Supporting Information

Soft Robotic Concepts in Catheter Design: an On-demand Fouling-release Urinary Catheter

Vrad Levering, Qiming Wang, Phanindhar Shivapooja, Prof. Xuanhe Zhao, and Prof. Gabriel P. López**

Figure S1. Growth and characterization of mature *P. mirabilis* crystalline biofilms on flat silicone substrates. (a) Schematic of the flow system. The silicone samples were submerged in (b) the modified drip flow reactor [1] and inoculated with a 4 hour culture of *P. mirabilis.* After allowing the bacteria to adhere for 1 hour, artificial urine with 1% tryptic soy broth was pumped at 0.5 mL min^{-1} through the drip flow reactor and over the flat silicone samples. The reactor was maintained at 37°C by mini-incubator. A mature crystalline biofilm grew over approximately 42 hours. (c) SEM of the resultant planar biofilm shows large crystals and microcrystal aggregates typical of mature *P. mirabilis* biofilms observed in catheters removed from infected patients.[2]

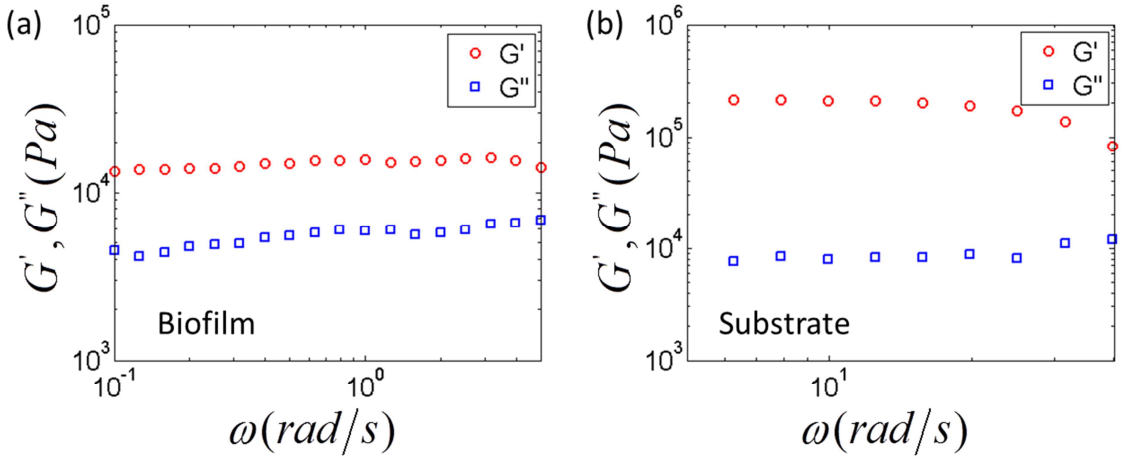

Figure S2. Storage modulus $G^{'}$ and loss modulus $G^{"}$ of mature *P. mirabilis* crystalline biofilms and the silicone substrate as a function of frequency. (a) *P. mirabilis* crystalline biofilms appeared to demonstrate predominantly elastic properties; the storage modulus was higher than the loss modulus and was relatively constant over the frequency range tested.[3] (b) Storage and loss moduli of silicone substrate.

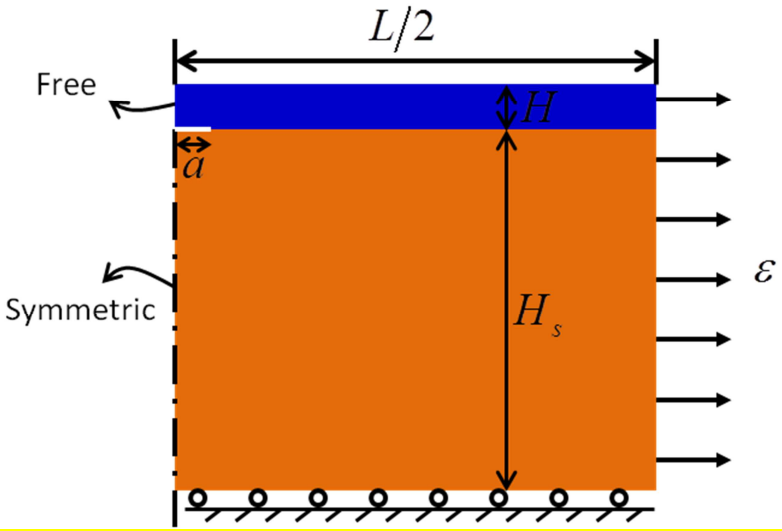

Figure S3. Schematic illustration of the boundary conditions for the finite element model for calculating energy release rate in Figure 3c. H is the thickness of the biofilm, H_f is the thickness of the substrate, L is the crack width illustrated in Figure 3b, a is the crack length on the biofilm-substrate interface, and ε is the applied strain. Boundary and load conditions include: symmetric boundary condition on the left surface of the substrate, a sliding condition on the bottom of the substrate, a horizontal displacement of $\varepsilon L/2$ applied on the right surfaces of the biofilm and the substrate, and free boundaries on other surfaces.

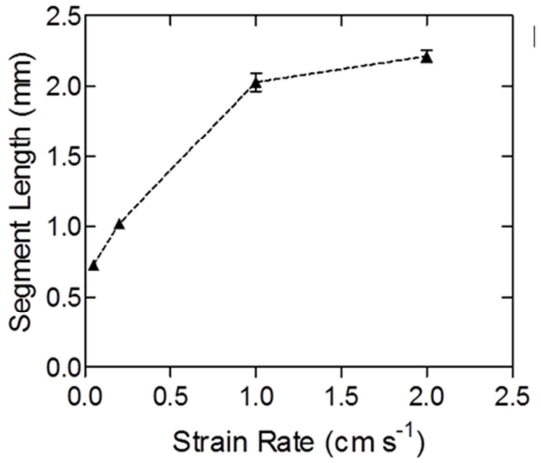

Figure S4. Segment length increases with increasing strain rate. Segment length from representative images at 100% strain (such as those in **Figure 3 B** and **C**). Five lines were drawn lengthwise (equally spaced along the width of the sample) on each image, and segment length was measured along the lines using ImageJ. Error bars provide the standard error of the mean of greater than 30 measurements per image.

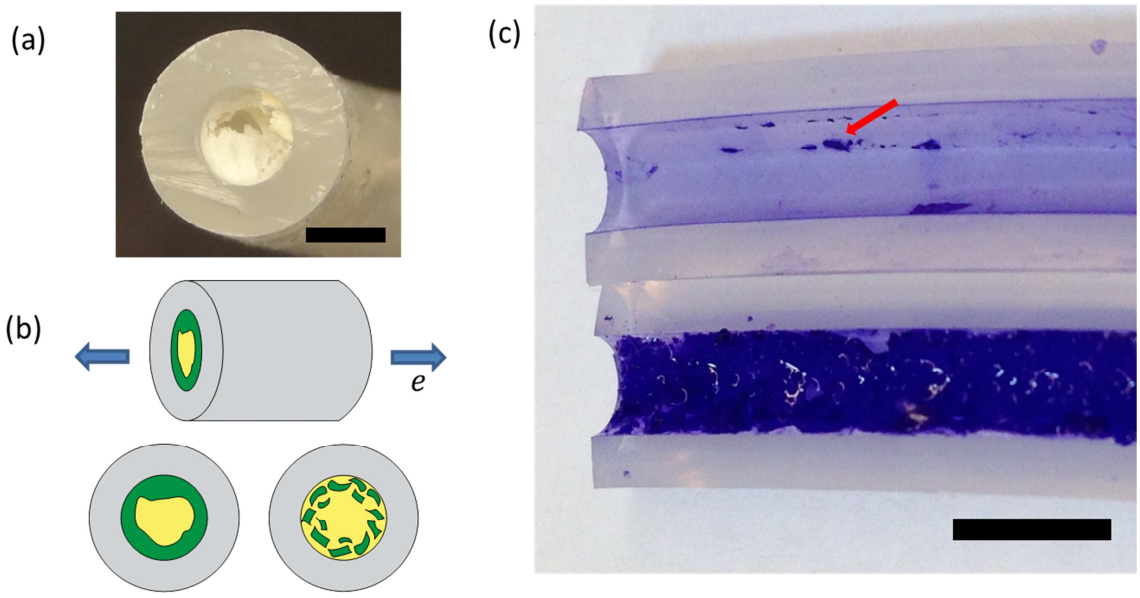

Figure S5. Debonding of mature *P. mirabilis* crystalline biofilms via applied strain to silicone tubing substrates. (a) Representative image of crystalline biofilm occluding a portion of silicone tubing. Using similar growth methods to the flat configuration, mature crystalline biofilm was grown in silicone tubing (6.35mm inner diameter silicone tubing, VWR). Bar indicates 2.5 mm. (b) Diagram of how tensile strain applied to substrate debonds a biofilm within a tube. Unidirectional strain was applied axially. The cross section on the left represents a tube with biofilm grown on the main lumen; the cross section on the right represents the same tube after axial strain was applied to the substrate. Biofilm becomes debonded from the luminal surface and available for easy removal via rinse. (c) Image of sliced tubing sample subjected to 50% strain 10 times (top) and unstrained control (bottom) after rinsing. Arrow indicates example of remaining islands of biofilm of partial-thickness. Strained samples were stretched at 1.7 cm s^{-1} using a LRX tensile tester. Samples were then rinsed at 4 mL min^{-1} before crystal violet staining. SEM comparison of flat and tubular silicone surfaces used for these experiments confirmed similar surface topographies. Scale bar indicates 5 mm.

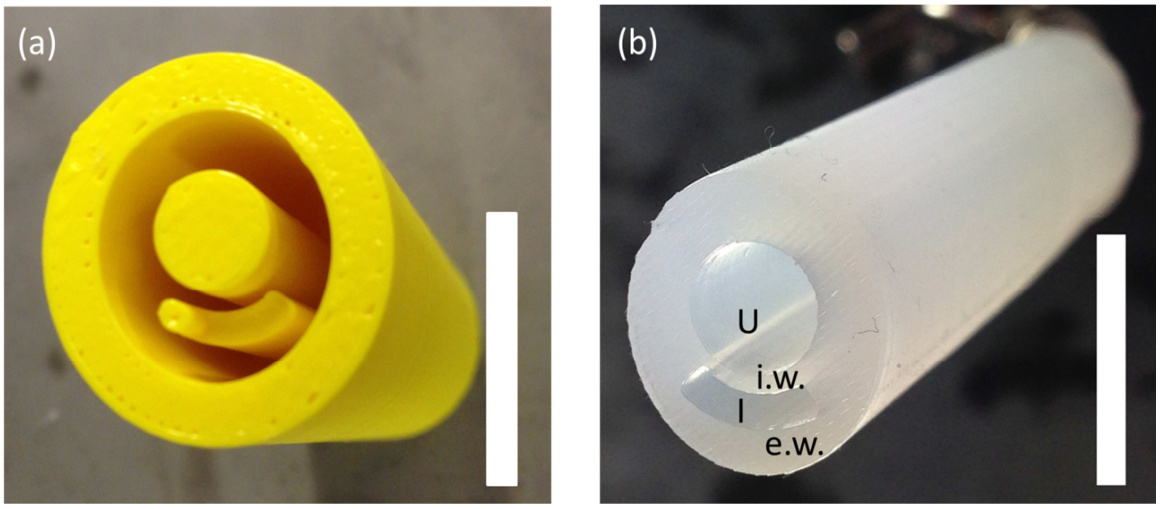

Figure S6. Construction of an active fouling release, proof-of-concept prototype of a section of silicone urinary catheter. (a) 3D printed mold patterns were generated using Solidworks 2011 and then printed on a Dimension sst 1200es 3D printer. Silicone (Dragon Skin 0020 or Ecoflex 0050) was poured into the mold and (b) resultant silicone prototypes were removed from the mold upon curing. "U" denotes the main urine drainage lumen, "I" denotes the inflation lumen, "i.w." denotes the inflation wall, and "e.w" denotes the external wall. The inflation lumen was sealed at the ends of the prototypes before experimentation. When using Dragon Skin 0020 silicone, the ratio of external wall to inflation wall thicknesses shown (approximately 3:1) was sufficient to direct inflation inwards. When using Ecoflex 0050 silicone, prototypes required an additional inelastic sheath to prevent bulging of the external wall. Ecoflex 0050 was chosen for *in vitro* biofilm testing due to its superior pour performance and consistently successful molding. Scale bar represents 1 cm.

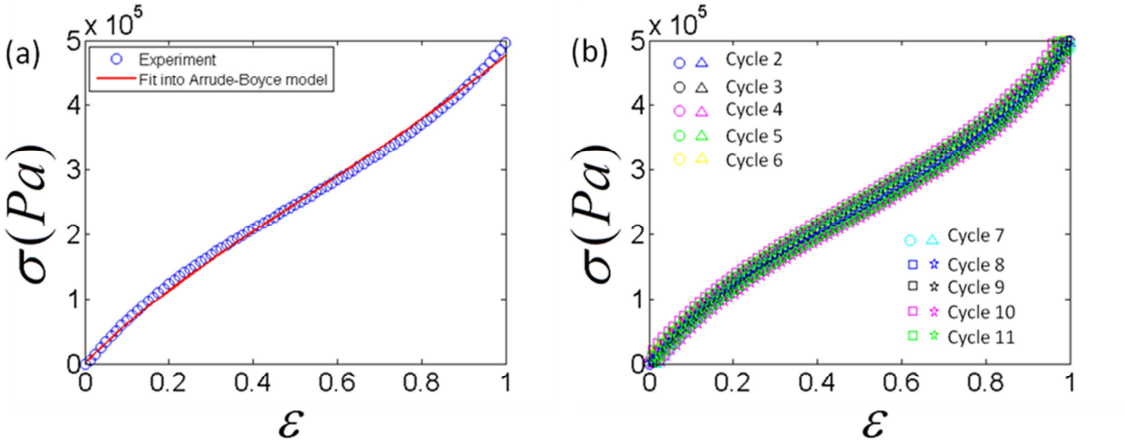

Figure S7. (a) Nominal stress *vs*. strain curve of Dragon skin 0020 was fit to the Arrude-Boyce model, $\sigma = \mu_s(\lambda - \lambda^{-2})(1 + \frac{I}{5n} + \frac{11I^2}{175n^2} + \cdots)$, where σ and $\lambda = 1 + \varepsilon$ are the nominal stress and stretch for uniaxial tension, $I = \lambda^2 + 2\lambda^{-1}$, and n is a parameter that accounts for the stiffening effect.[4] The fitted shear modulus is μ_s =221 kPa, and the exponent was fitted as n = 0.27. (b) Cycling test of Dragon skin 0020 shows negligible hysteresis after the first strain loading cycle. Silicone samples (flat and proof-of-concept prototypes) were prestrained or preactuated at least once prior to experimentation.

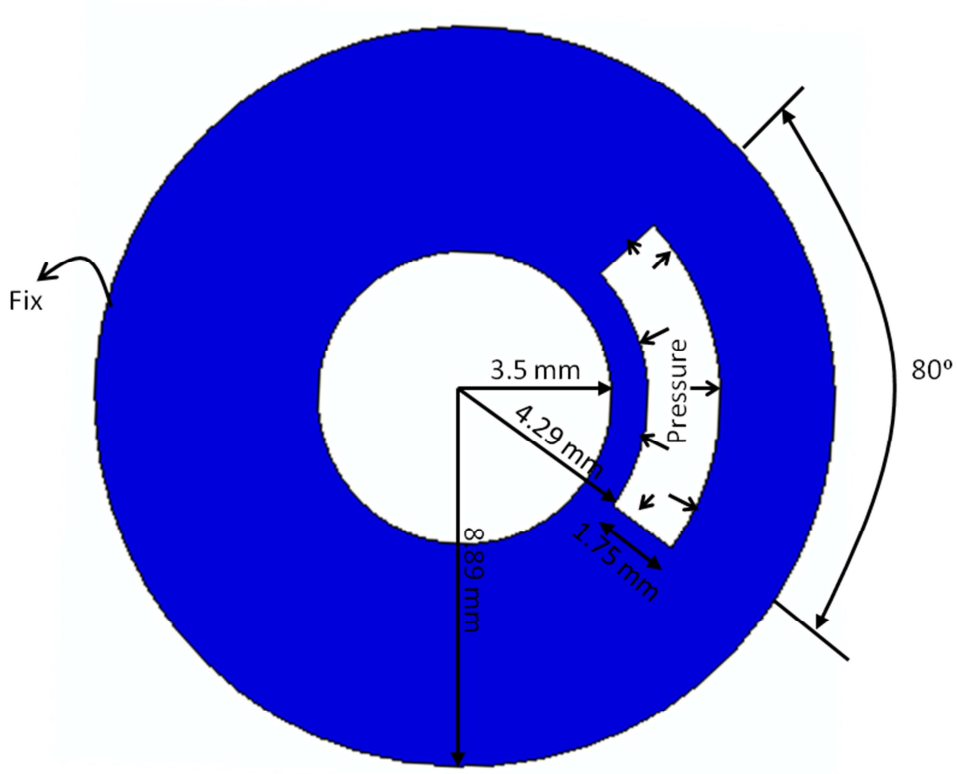

Figure S8. Schematic illustration of the boundary conditions for the finite element model for calculating strain at the luminal surface of proof-of-concept prototypes (Dragon Skin 0020) in Figures 4c and 4d. The outer surface the model was fixed, and pressure was applied on the inner surface of the inflation lumen.

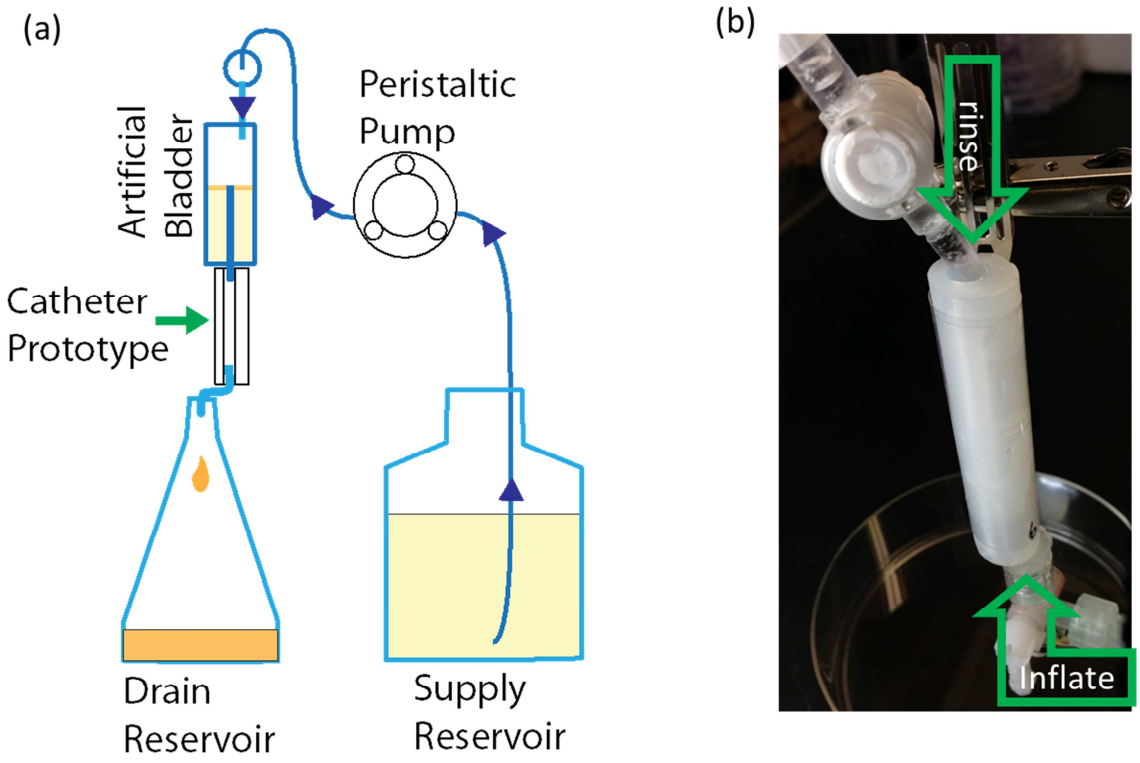

Figure S9. Biofilm growth and testing setup for urinary catheter proof-of-concept prototypes. (a) Schematic of biofilm growth system that uses an "artificial bladder" [5] to supply infected urine to the proof-of-concept prototypes. The artificial bladder is a vessel modified with a glass tube penetrating the bottom and extending approximately 4 cm into the vessel, which thereby maintains a residual volume of 30 mL in the artificial bladder. The artificial bladder and prototypes were inoculated with a 4 hour culture of *P. mirabilis.* After allowing the bacteria to adhere for 1 hour, artificial urine with 1% tryptic soy broth was pumped at 0.5 mL min^{-1} into the artificial bladder and through the prototypes. As artificial urine media was fed into the artificial bladder the media overflowed into the glass tube, where it then fed down the main drainage lumen of the catheter prototypes. The bladder and prototypes were maintained at 37°C by mini-incubator. A mature crystalline biofilm grew over approximately 42 hours. (b) Rinsing test setup for prototypes after biofiolm growth. After carefully removing the prototypes from the biofilm growth system, a DI water rinse supplied at 4 mL min^{-1} flowed downward through the prototype main urine drainage lumen for 1 minute. Prototypes designated for actuation were hydraulically inflated 10 times at a rate of 0.1 s^{-1} approximately 30 seconds into the rinse. Hydraulic inflation was applied to the inflation lumen through an inflation port fixture on the bottom end of the prototype. The rinse effluent was collected for analysis and the prototype was then removed for inspection.

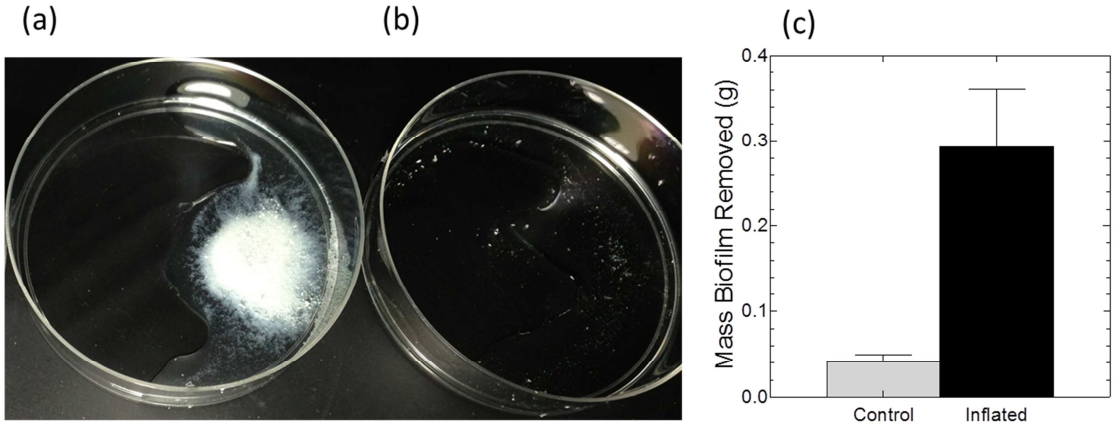

Figure S10. Dramatic release of biofilm into the effluent from inflated proof-of-concept prototype urinary catheters. (a) Representative optical image of effluent from 3 prototypes each actuated 10x during rinsing (4 mL min^{-1} through the prototype main urine drainage lumen for 1 minute); effluent contained visible biofilm debris. (b) Representative effluent from 2 un-actuated control prototypes had minimal biofilm debris, implying that control prototypes retained biofilm after rinsing alone. (c) The effluent was collected, centrifuged, and the excess liquid was aspirated. Figure shows hydrated mass of biofilm collected. Data represents mean ± standard error of the mean.

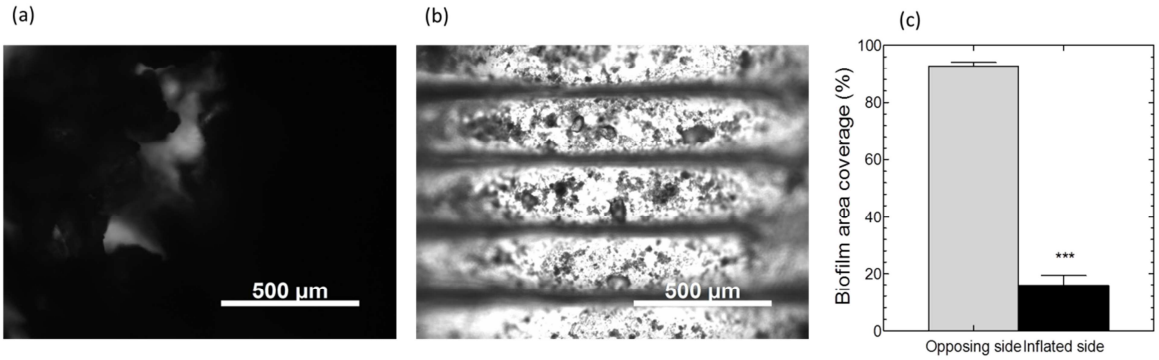

Figure S11. Microscopic observation of debonding of biofilm from the main urine drainage lumen of catheter section prototypes. (a) Microscope image of surface of control prototype main lumen covered with biofilm after rinsing and (b) Microscope image of inflated prototype main lumen with biofilm removed after inflation and rinsing. Note: Horizontal bars visible across the inflation wall are "ribs" around the lumen that are due to the 3D printing process used to form the mold. (c) ImageJ was used to analyze the images, and statistical comparison to the opposing side of the catheter lumen showed that inflation debonded the biofilm from the area of the luminal wall subjected to inflation. Comparison was statistically significant both with ($p<0.006$) and without ($p<0.0009$) rib artifacts removed from images. Data represents mean ± standard error of the mean, N=4.

Table S1. Hydraulic inflation profile for proof-of-concept prototypes of urinary catheter sections.

Inflation Volume (mL water)	Strain (%)
0	**0.0**
1	**13.0**
1.3	**34.7**
1.6	**38.8**
1.7	**39.1**

References

[1] D. M. Goeres, L. R. Loetterle, M. A. Hamilton, R. Murga, D. W. Kirby, R. M. Donlan, *Microbiology* **2005**, *151*, 757-762.

[2] D. J. Stickler, S. D. Morgan, *J Hosp Infect* **2008**, *69*, 350-360.

[3] M. Bol, A. E. Ehret, A. Bolea Albero, J. Hellriegel, R. Krull, *Crit Rev Biotechnol* **2013**, *33*, 145-171.

[4] J. S. Bergstrom, M. C. Boyce, *Rubber Chemistry and Technology* **1999**, *72*, 633-656.

[5] D. J. Stickler, N. S. Morris, C. Winters, *Methods Enzymol* **1999**, *310*, 494-501.